Downhole electric heater with high heating efficiency for oil shale exploitation based on a double-shell structure

Author(s): Wang, Zhendong; Lü, Xiaoshu; Li, Qiang; Sun, Youhong; Wang, Yuan; Deng, Sunhua; Guo, Wei

Title: Downhole electric heater with high heating efficiency for oil shale exploitation based on a double-shell structure

Year: 2020

Version: Accepted manuscript

Please cite the original version:

Wang, Z., Lü, X., Li, Q., Sun, Y., Wang, Y., Deng, S. & Guo, W. (2020). Downhole electric heater with high heating efficiency for oil shale exploitation based on a double-shell structure. *Energy* 211. https://doi.org/10.1016/j.energy.2020.118539

Downhole electric heater with high heating efficiency for oil shale exploitation based on a double-shell structure

Zhendong Wang[a,b,c], Xiaoshu Lü[a,b,e,f], Qiang Li[a,b,c], Youhong Sun[b,c,d], Yuan Wang[a,b,c], Sunhua Deng[a,b,c], Wei Guo[a,b,c*]

a College of Construction Engineering, Jilin University, Changchun 130021, China

b National-Local Joint Engineering Laboratory of In situ Conversion, Drilling and Exploitation Technology for Oil Shale, Jilin University, Changchun, 130021, China

c Key Lab of Ministry of Natural Resources for Drilling and Exploitation Technology in Complex Conditions, Jilin University, Changchun 130021, China

d China University of Geosciences, Beijing, 100083, China

e Department of Electrical Engineering and Energy Technology, University of Vaasa, FIN-65200 Vaasa, Finland

f Department of Civil and Structural Engineering, School of Engineering, Aalto University, P.O.Box 12100, FIN-02015, Finland

Wei Guo*; E-mail: guowei6981@jlu.edu.cn

Abstract: To improve the heating efficiency of the downhole electric heaters used in oil shale exploitation, double-shell downhole electric heaters with continuous helical baffles (DS-DEHs) were developed in this study. These heaters reduce heat loss generated by the shell of single-shell downhole electric heaters with continuous helical baffles (SS-DEHs) and reuse the heat loss by driving air flows through outer and inner shell-passes in sequence. Two types of DS-DEHs with three different helical pitches were experimentally studied, and SS-DEHs were set as the control. The results indicated that the effect of mass flow rate on the heating rate is greater than that of heating power. Forced convection heat transfer is the major heat transfer mode in heater shell-side, and the contribution of shell-side radiant heat transfer mainly depends on the helical pitch, then on the heating power and mass flow rate. Additionally, the heat loss generated by heater shell is mainly dissipated in the form of radiation. The total heat loss of the DS-DEH is 87.16%-96.41% lower than that of the SS-DEH, and its heating efficiency is 1.06-1.17 times than that of SS-DEH, indicating that the double-shell structure can effectively improve the heating efficiency of downhole electric heaters. These findings are beneficial for designing energy-efficient downhole electric heaters used in oil shale exploitation.

Keywords: In situ pyrolysis; Downhole electric heater; Double-shell structure; Outlet temperature response; Heating efficiency

1. Introduction

Unconventional reservoirs, such as high-viscosity oil deposits and oil shale, will be the main fossil energy consumed in the future [1,2]. Compared with highly mature reservoirs, organic matters (kerogen) in unconventional reservoirs have a low degree of thermal evolution and require heat treatment before they can be utilised [3,4]. The traditional heat treatment methods of unconventional reservoirs include steam flooding, steam huff and puff, and superheated steam exploitation [5,6]. Generating high-temperature fluids with downhole electric heaters can reduce heat losses along heat insulation pipelines [7].

Previous studies on downhole electric heaters in heavy oil and oil shale have focused on heating reservoirs through heat conduction using electrodes. However, heating unconventional reservoirs with electrodes is time consuming owing to the lower heat transfer efficiency of heat conduction, which is caused by the small heat transfer area of bare electrodes. Additionally, bare electrodes without an enhanced heat transfer structure are prone to thermal damage owing to local hot spot under high heat flux; therefore, previously investigated electric heaters [8-10] are not suitable for quickly generating large amounts of high-temperature fluids. The downhole electric heaters with continuous helical baffles proposed by Guo [7] are a good option for efficiently heating oil shale using high-temperature fluids, which heat oil shale through thermal convection. Oil shale is a type of rock with low thermal conductivity. For heating oil shale, convective heating is more effective than heat conduction.

The heating efficiency of downhole electric heaters directly determines whether oil shale can be heated underground, and the heating time required for the generation of oil and gas [11]. The heat source of downhole electric heaters is electric heating rods. Therefore, the first step toward improving the heating efficiency of a heater is to increase the amount of heat absorbed by the shell-side air, i.e. designing a downhole heater that has an efficient heat transfer enhancement structure, which has been studied in previous studies; the second step is to weaken the heat dissipated by the heater shell, i.e. designing a downhole heater with a novel thermal insulation structure to reduce the heat loss generated by heater shell, which is the focus of this study.

Many scholars have focused on improving the thermal performance of heat exchangers by changing the geometric parameters of enhanced heat transfer structures (baffle and heat transfer tube type); however, few have considered reducing the heat dissipated by heat exchanger shells. Yang [12] simulated a heat transfer structure with different combined parameters of folded and segmental baffles. According to the study, the comprehensive performance of a heat transfer structure with a smaller helical pitch or shorter projection length of an inclined section of folded baffles is better than other schemes. Furthermore, the thermal performance of the helical heat transfer structure is better than that of the segmental one in the same test conditions. Wang [13] investigated the flow and heat transfer performances of double-shell rod baffle heat exchangers. The simulation results indicated that the thermal performance of the outlet zone can be improved effectively 13%-29% by setting the guide shell in the shell-side outlet zone. From the experiments, they found that the comprehensive performance of double-shell baffle heat exchanger was 14.4–24.3% higher than that of single-shell baffle rod heat exchangers. Wang [14] simulated a double-pipe heat exchanger with an outward helically corrugated tube and discovered that the heat transfer performance of the heat exchanger varied linearly with the diameter of the heat exchanger shell. When shell inner diameter was 38 mm, the heat exchanger achieved the best comprehensive performance. Ji [15] simulated the heat transfer performance of a double-shell helical baffle heat exchanger and indicated that the shell-side heat transfer coefficient of the double-shell heat exchanger was 14%-25% higher than that of segmental heat exchanger. Yang [16] studied multiple shell heat exchangers with continuous helical baffles, and discovered that the thermal performance of the novel heat exchanger was higher than that of multiple shell heat exchangers with segmental baffles under the same pressure drop.

Previous studies [12-16] were primarily focused on improving the heat utilisation efficiency of heat exchangers through combined baffles, double pipes, double shells and combined multiple heat transfer structures, with little consideration of the outlet temperature response and shell-side radiative heat transfer characteristics, and the heat loss generated by the heater shell. Furthermore, the temperature response characteristic of the downhole heater is related to the pyrolysis temperature and decomposition-activation energy of oil shale around heating well [17-19]. In addition, during operation, the shell of the downhole heater always reaches high temperatures, which cannot be effectively reduced by using thermal insulation materials. Regarding the heat exchangers used to cool hot fluids in oil refineries, researchers have primarily focused on the heat transfer capacity of enhanced heat transfer structures, that is, the amount of heat absorbed by the coolant from hot fluids [12-16], whereas little attention has been paid to improving the utilisation ratio of heat absorbed by the shell-side coolant [20-22], which can be achieved by reducing the heat exchanger shell temperature.

However, in the in situ exploitation of unconventional reservoirs, when a downhole electric heater is placed in a heating well together with a packer at its outlet, a large amount of heat lost by heater shell cannot be effectively utilised. A double-shell downhole electric heater with continuous helical baffles (DS-DEH) drives the air flows through the outer and inner shell-passes in sequence, which not only reduces the thermal radiant energy and natural convection heat transfer of a single-shell downhole electric heater with continuous helical baffles (SS-DEH), but also reuses heat dissipated by the shell of the SS-DEH to preheat the outer shell-pass air.

In this study, a novel double-shell structure was designed to improve the heating efficiency of the downhole electric heater. In addition, the feasibility of the double-shell structure in improving the heating efficiency of the downhole heater was verified by comparing the thermal performance with the outlet temperature response characteristics and analysing the heating efficiency of the SS-DEH and DS-DEH.

2. Experimental investigation

2.1. Experimental apparatus

Three types of downhole heaters were tested in the experiment: 1. SS-DEH; 2. Parallel double-shell downhole electric heater with continuous helical baffles (PDS-DEH), in which the inlet of the heater is on the side of the SS-DEH inlet; and 3. Countercurrent double-shell downhole electric heater with continuous helical baffles (CDS-DEH), in which the inlet of the heater is on the side of the SS-DEH outlet. Fig. 1 shows the schematics of the air flow path and heat loss of the heater shell.

In this study, experiments were conducted on two types of DS-DEHs, each with three different pitches from 50 to 210 mm, and the SS-DEH with pitches of 50, 110, 210 mm as the contrast. Except for the different pitches of the continuous helical baffle, the remaining parameters of the same heater type were identical. The details of the tested downhole electric heater are presented in Table 1. In all tests, the heaters were placed vertically because the downhole heater was installed vertically in the heating well during oil shale in situ pyrolysis.

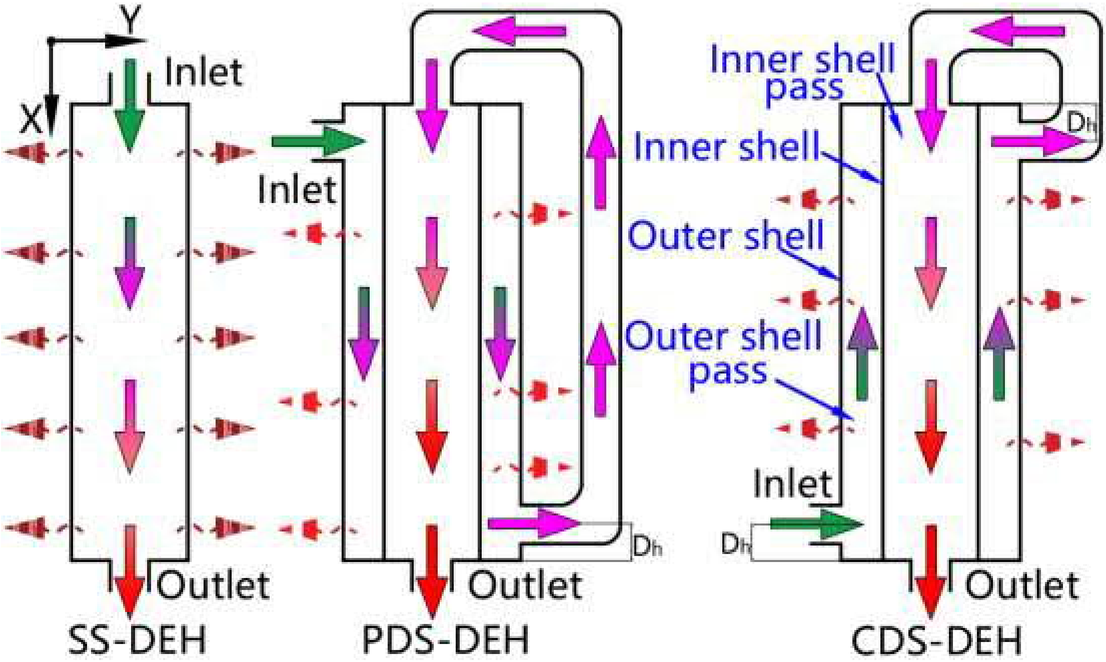

Fig. 1. The schematics of the air flow path and heat loss of the heater shell

Table 1 Details of heater

Item	Dimensions and description	
	SS-DEH	DS-DEH
(Inner) Shell inside / outside diameter (mm)	131/139	131/139
Outer Shell inside / outside diameter (mm)	---	188/208
(Inner & outer) Shell length (mm)	1100	1100
Inlet & outlet nozzle inside diameter (mm)	25.4	25.4
Inlet & outlet tube length (mm)	350	350
Helical pitch (mm)	50, 110, 210	50, 110, 210
Helical baffle thickness (mm)	2	2
Helical baffle length (mm)	1000	1000
Central tube outside diameter (mm)	32	32
Central tube length (mm)	1000	1000
Heating rode outside diameter (mm)	16	16
Effective length of heating rod (mm)	1000	1000
Heating rod length (mm)	1050	1050
Number of heating rods	6	6
Distribution form of heating rods	Evenly distributed on 80 mm diameter circle	
Distance D_h (mm)	25	25

2.2. Experimental system

The test system comprises three separate parts: the compressed air supply system, electronic control system, and data collection system. Fig. 2 shows the schematics of test system. The compressor provided compressed air; subsequently, the oil and water in the compressed air were filtered through a tertiary filter before being injected into downhole heater. The electronic control system controlled the on and off of the heater and the heating power. The on/off of the downhole heater was controlled by the temperature control meter. In addition, heating power was controlled using the power regulator. Temperature and pressure data were collected using a paperless recorder. Fig. 3 provides the photograph of the test system, in which a single-shell heater was tested. In this test, platinum-resistant thermometers (PT100) were used in the inlet, outlet, and heater shell, whereas K-type thermocouples were attached to the electric-heating-rod surface. The shell-side resistance was measured using capacitive differential pressure sensors. For heaters with the same helical pitch, the layout parameters of heating rod temperature sensors were the same. All the tested heaters have the same temperature measurement locations on the heater shell. Table 2 shows the layout parameters of the heating rod and heater shell temperature sensors.

Table 2 Layout parameters of heating rod and heater shell temperature sensors

Item	Temperature sensor positions on heating rod and heater shell (mm)
Heaters-50	50, 190, 390, 590, 790, 990
Heaters-110	100, 210, 320, 430, 540, 650, 760, 870, 980
Heaters-210	120, 330, 540, 750, 960
Heater shell	80, 180, 280, 380, 480, 580, 680, 780, 880, 980, 1080

Here, Heaters-50 represents all the tested heaters, which include PDS-DEH, CDS-DEH and SS-DEH, with the helical pitch of 50 mm, and the numbers 50, 110, and 210 represent the helical pitch of the heater.

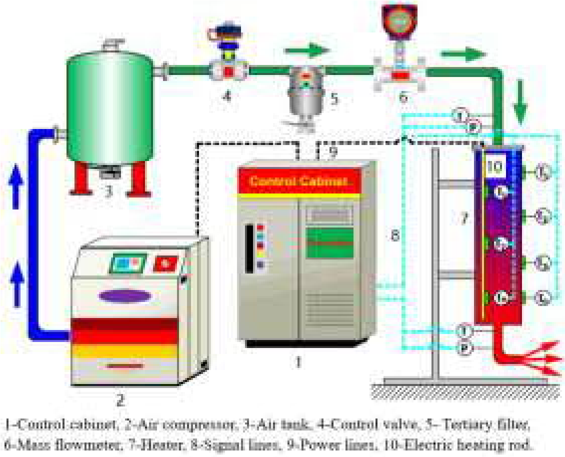

Fig. 2. Schematics of the test system

Fig. 3. Photograph of the test system

2.3. Experimental scheme

In the experiments, the outlets of SS-DEH, PDS-DEH, and CDS-DEH were set as free flowing. In addition, two schemes were applied in the test. The constant heating power scheme was used for analysing the outlet temperature response characteristics, thermal performance, and heating efficiency. In addition, a series of tests involving three heating power values and five mass flow rates was conducted on each heater. A constant outlet temperature scheme was applied to measure the temperatures of the heating rod and heater shell when M=0.016 kg/s and T_{out}=250 °C.

2.4. Data processing

2.4.1. Natural convection and thermal radiation of heater shell

To investigate and validate the calculation of the characteristics of combined heat transfer of radiation and convection in the heater shell, temperature sensors are placed in the surface of the heater shell. Because the temperature values of heater shell varied significantly along X-axis, heater shell was divided into 11 sections by 11 temperature measuring points to calculate the heat transfer of radiation and natural convection generated by heater shell. The total heat loss generated by heater shell is the sum of heat loss of the 11-section heater shell.

The total heat loss of heater shell can be expressed as:

$$Q_{thl} = Q_{conv} + Q_{rhs} \tag{1}$$

The formula to calculate the natural convective heat transfer is:

$$Q_{conv} = \sum_{i=1}^{11} Q_{ci} \tag{2}$$

where Q_{ci} is the heat loss by each section of heater shell, which can be calculated using Eq. (3) [16,24]:

$$Q_{ci} = h_{hs} A_{hs} \Delta t_{conv} \tag{3}$$

where h_{hs} is the heat transfer coefficient of heater shell, A_{hs} is the outer surface area of heater shell. Table 3 shows the calculation area of natural convection and thermal radiation.

Table 3 The calculation area of natural convection and thermal radiation

i	1	2-10	11
A_{hs}/m^2	0.05225	0.06531	0.04572

The natural convective heat transfer difference is defined as:

$$\Delta t_{conv} = T_{hs} - T_{amt} \tag{4}$$

where T_{hs} and T_{amt} are the temperatures of heater shell and ambient air, respectively, and T_{amt} kept 17.0 ($\pm$0.5) ℃.

The natural convective heat transfer coefficient of heater shell is defined as follows [25,26]:

$$h_{hs} = \frac{\lambda_{amt} N_u}{L_{hs}} \tag{5}$$

where L_{hs} is the length of heater shell, λ_{amt} is the thermal conductivity of ambient air.

The Nusselt number of heater shell boundary layer is expressed as [27]:

$$N_u = CR_a^n \tag{6}$$

where C = 0.59, and n= 0.25.

The Rayleigh number is calculated as [27]:

$$R_a = G_r P_r = \frac{g\beta\Delta t_{conv} L_{hs}^3 P_r}{\mathrm{v}_{amt}^2} \tag{7}$$

where g is the acceleration of gravity, P_r and v_{amt} are the Prandtl number and kinematic viscosity of ambient air, respectively.

The coefficient of thermal expansion can be expressed as [27]:

$$\beta = \frac{2}{T_{hs}+T_{amt}} \tag{8}$$

The thermal radiant energy of the heater shell is defined as [28,29]

$$Q_{rhs} = \sum_{i=1}^{11}\{\varepsilon A_{hs}\sigma(T_{hs}^4 - T_{amt}^4)\} \tag{9}$$

where ε is the thermal radiation emissivity of the heater shell, which can be found in Table 4; σ is the Stefan-Boltzmann constant, i.e. $\sigma = 5.67 * 10^{-8}$ (W/(m^2·K^4)).

Table 4 The thermal radiation emissivity of heating rod and heater shell

ε	0.4	0.6	0.8	0.85	0.9
Temperature/°C	23.22-63.16	64.01-91.86	92.49-160.66	161.37-329.75	330.5-469.61

The heat loss relative error of heater shell α between theoretical calculation and experimental result is defined as:

$$\alpha = \frac{Q_{thl}-Q_{hbhl}}{Q_{hbhl}} \times 100\% \tag{10}$$

$$Q_{hbhl} = P - M(F_{out} - F_{in}) \tag{11}$$

where Q_{hbhl} is the heat loss of heater shell based on the principle of heat balance.

The theoretical calculation of heat loss by heater shell appears to agree reasonably well with the experimental data with a deviation of ±3.87%.

2.4.2. Heat transfer enhancement analysis of heater

The heater with double-shell structure improves its heating efficiency by changing the flow path of the shell-side air. The inner shell-pass of DS-DEH is provided with an enhanced heat transfer structure, while the outer shell-pass has no enhanced heat transfer structure. The enhanced heat transfer performance of DS-DEH is mainly related to the inner shell-pass. To effectively compare the enhanced heat transfer performances of DS-DEH and SS-DEH, heaters adopt the same calculation formula of enhanced heat transfer.

To reflect the influence of the variation of shell-side air thermophysical parameters, the average temperature at the inlet and outlet of heater is taken as the characteristic temperature of shell-side air.

According to Eq. (12), the Nusselt number of heating rod boundary layer under experimental condition can be calculated [31-33].

$$N_u = \frac{h_{hr} d_{hr}}{\lambda_s} \tag{12}$$

where λ_s is the thermal conductivity of shell-side air, d_{hr} is the outer diameter of heating rod.

Based on experimental data, the convection heat transfer coefficient (h_{hr}) of heating rod surface is calculated by the following formula:

$$h_{hr} = \frac{(F_{out} - F_{in})M - Q_{rhr}}{A_{ehr}\Delta t_e} \tag{13}$$

$$A_{ehr} = 6\pi d_{hr} L_{ehr} \tag{14}$$

Based on the layout parameters of heating rod temperature sensors in Table 2, the thermal radiant energy of heating rod Q_{rhr} is calculated in sections, Table 5 shows the calculation area of thermal radiation on heating rod.

$$Q_{rhr} = \sum_{i=1}^{6/10} \{\varepsilon A_{ehr} \sigma (T_{hr}^4 - T_{air}^4)\} \tag{15}$$

where F_{out} and F_{in} are the specific enthalpy of air at the outlet and inlet of heater, respectively; A_{ehr} is the heat transfer area based on effective length of heating rod, L_{ehr} is the effective length of heating rod.

Table 5 The calculation area of thermal radiation on heating rod

i	1	2	$3-5$	6	7-9	10
Heaters-50/m^2	0.01206	0.06032	0.06032	0.04825	---	---
Heaters-110/m^2	0.00905	0.02413	0.03318	0.03318	0.03318	0.03619
Heaters-210/m^2	0.00905	0.04373	0.06333	0.05881	---	---

The logarithmic heat transfer temperature difference is defined as [30]:

$$\Delta t_e = \frac{\Delta t_{max} - \Delta t_{min}}{ln\frac{\Delta t_{max}}{\Delta t_{min}}} \tag{16}$$

where Δt_{max} is the difference between the heating rod temperature at 1050 mm and the outlet air temperature; Δt_{min} is the difference between the heating rod surface temperature at 50 mm and the inlet air temperature.

When the downhole electric heater operates in heating well, the maximal temperatures of heating rod under the corresponding operating conditions can be calculated by the regression parameters in Table 7.

The Nusselt number of heating rod boundary layer used to calculate the regression parameters is defined as [31-33]:

$$N_u = C R_e^m P_r^{\frac{1}{3}} \tag{17}$$

The Reynolds number is expressed as:

$$R_e = \frac{L_{cl} U_s \rho_s}{\mu_s} \tag{18}$$

$$U_s = \frac{M}{\rho_s A_{min}} \tag{19}$$

where L_{cl} is the characteristic length of shell-side, and is taken as the outer diameter of heating rod d_{hr}, U_s is the shell-side specific velocity, P_r, ρ_s and μ_s are the Prandtl number, density and dynamic viscosity of shell-side air, respectively.

The minimal free-flow area can be expressed as [22]:

$$A_{min} = 0.5B\cos\theta\,(d_{hs} - d_{ct} - 2d_{hr}) \tag{20}$$

where B is the helical pitch, θ is the helix angle, d_{hs} is the inner diameter of SS-DEH shell; d_{ct} is the outer diameter of central tube.

The friction factor is defined in Eq. (21).

$$f = \frac{\Delta P}{2\rho_s U_s^2} \cdot \frac{d_{hr}}{L_{ehr}} \tag{21}$$

where L_{ehr} is the effective length of heating rod.

The comprehensive performance index is expressed as:

$$\varphi = \frac{N_u}{f^{\frac{1}{3}}} \tag{22}$$

The heating efficiency is expressed as:

$$\eta = \frac{(F_{out}-F_{in})M}{(F_{out}-F_{in})M+Q_{thl}} \times 100\% \tag{23}$$

2.5 Experimental uncertainty

The experimental uncertainty of this study was obtained using the following equation [34,35]:

$$W_R = \sqrt{(\frac{\partial R}{\partial X_1} W_{x_1})^2 + (\frac{\partial R}{\partial X_2} W_{x_2})^2 \dots\dots + (\frac{\partial R}{\partial X_n} W_{x_n})^2} \tag{24}$$

where $W_R = f(x_1, x_2, \dots, x_n)$, and x_n is a variable affecting R.

In this study, the relative uncertainties of the directly measured parameters and the thermal radiant energy Q_{rad}, total heat loss Q_{thl} and heating efficiency η are provided in Table 6.

Table 6 Experimental uncertainties

Uncertainty item	Symbol	Unit	Value
Heating power	W_P	%	±(1.00-1.25)
Mass flow rate	W_M	%	±(0.13-0.25)
Heating rod temperature	W_T	%	±(0.20-0.24)
Inlet temperature	$W_{T_{in}}$	%	±(0.18-0.23)
Outlet temperature	$W_{T_{out}}$	%	±(0.14-0.20)
Thermal radiant energy	$W_{Q_{rad}}$	%	±(3.76-6.13)
Total heat loss	$W_{Q_{thl}}$	%	±(1.46-2.35)
Heating efficiency	W_η	%	±(0.11-0.18)

3. Results and discussion

Heaters with the same shell structure have the same size but different helical pitch values. Therefore, the heater shell structure, mass flow rate M, heating power P, and helical pitch values are independent variables used to study the performance of the double-shell and single-shell heaters. Additionally, the average value of each physical quantity is used to explore its variation characteristics.

3.1 Outlet temperature response characteristics

The downhole heater is used to heat oil shale underground. The response rate of its outlet temperature reflects its heat transfer capability, which is related to the pyrolysis temperature and decomposition-activation energy of oil shale around heating well and subsequently to the oil yield of the oil shale blocks [17-19]. To speed up the heating of oil shale zone and to convert kerogen into more oil, the outlet temperature response characteristics of the downhole heater is investigated for the research of the optimal heating control strategy.

Fig. 4 shows the representative outlet temperature (T_{out}) response curve of the downhole heater. In stage 1, the outlet temperature rapidly, then the increase rate slowed down in stage 2 until stabilized in stage 3. Fig. 5 shows the heating rate of the downhole heater when the heating time is 3000 s. As shown in the figure, PDS-DEH-50 has the largest heating rate, whereas SS-DEH-50 has the smallest one. Fig. 6 presents the outlet temperature (T_{out}) variation trend of SS-DEH-210. Fig. 6 (a) shows that increasing the mass flow rate does not proportionally increase the amount of absorbed heat; Therefore, the heating rate, the time durations in stages 1 and 2, and the outlet temperature decreases. By contrast, the temperature difference increases with the increase of heating power; hence, the heating rate, time durations in stages 1 and 2, and outlet temperature increases. Additionally, with the decrease in the heating power and the increase in the mass flow rate, the time durations in stages 1 and 2 decreases. Furthermore, the effect of mass flow rate on heating rate is greater than that of heating power.

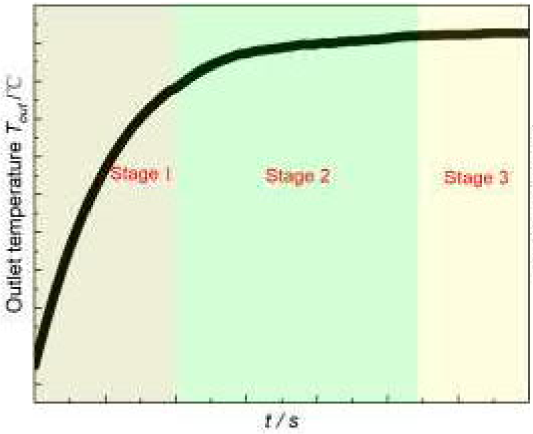

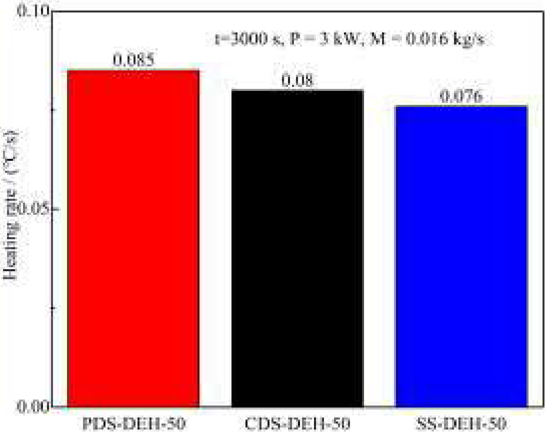

Fig. 4. The representative outlet temperature response curve

Fig. 5. The heating rate of heater

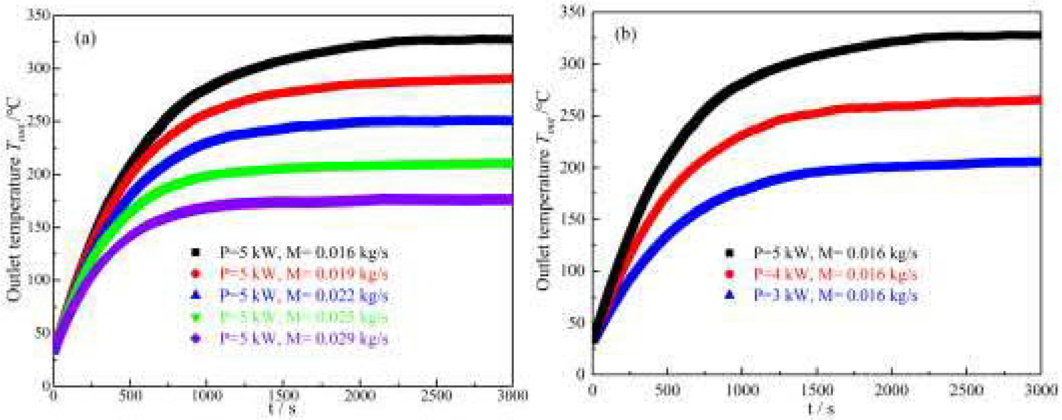

Fig. 6. The outlet temperature response curve versus mass flow rate and heating power

3.2. Comprehensive performance evaluation

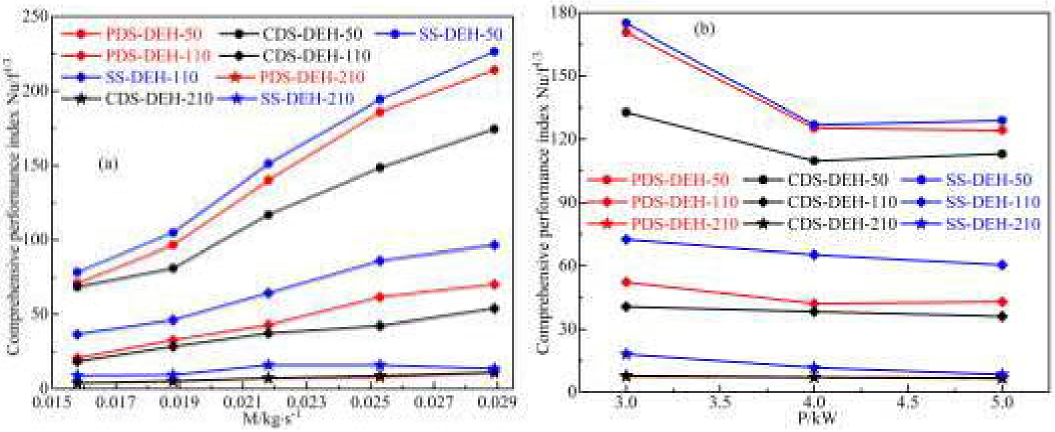

Fig. 7. Comprehensive performance index versus mass flow rate and heating power

Fig. 7 shows the comprehensive performance index versus mass flow rate and heating power. Compared with the SS-DEH, the Prandtl number of air decreases and the air viscosity increases after the air is heated in the outer shell-pass in the DS-DEH, therefore, the Nusselt number of the heater decreases. In addition, owing to the increase in air viscosity and the air flow path, the local differential pressure resistance and friction resistance of downhole heater increases simultaneously in the DS-DEH. These two mechanisms resulted in higher comprehensive performance index of the SS-DEH compared to that of the DS-DEH. Owing to the lower air temperature at the same location, the thermal performance of the PDS-DEH is higher than that of the CDS-DEH. When the helical pitch is small, the thermal performances of the PDS-DEH and SS-DEH are similar (e.g. those of SS-DEH-50 and PDS-DEH-50), however, when the helical pitch is large, the thermal performances of the CDS-DEH and PDS-DEH are similar. Moreover, the heater with a small helical pitch has small circulation area and a large Nusselt number, therefore, its thermal performance increases with the decrease in the helical pitch. As shown in Fig. 7 (a), the comprehensive performance index increases with the increase in the mass flow rate, and the smaller is the helical pitch, the more pronounced is the increase in the comprehensive performance index. As shown in Fig. 7 (b), the thermal performance of the SS-DEH decreases with heating power. When helical pitch is 50 mm, the thermal performance variation trend of the DS-DEH is the same as that of the SS-DEH. With the increase in the helical pitch, the heating power did not significantly affect the thermal performance of DS-DEH.

3.3. Heat transfer correlation

From Eq. 17, the following equation can be obtained:

$$\ln\left(N_u P_r^{-\frac{1}{3}}\right) = \mathrm{m}\ln(R_e) + \ln(C) \tag{25}$$

with the following linear regression form:

$$\mathrm{Y} = \mathrm{DX} + \mathrm{b} \tag{26}$$

where $X = \ln(Re)$, $Y = \ln\left(N_u P_r^{-\frac{1}{3}}\right)$, and $b = \ln(C)$. The linear regression curves of heat transfer correlation are shown in Fig. 8. The regression parameters listed in Table 7 are obtained from the fitting curves in Fig. 8.

When the downhole electric heater operates in heating well, the temperature sensors cannot be arranged on the electric heating rod owing to limitations of the heater sealing structure and the packer structure. To prevent high-temperature ablations of the electric heating rod, the maximal temperatures of heating rod under the corresponding operating conditions can be calculated using the regression parameters in Table 7.

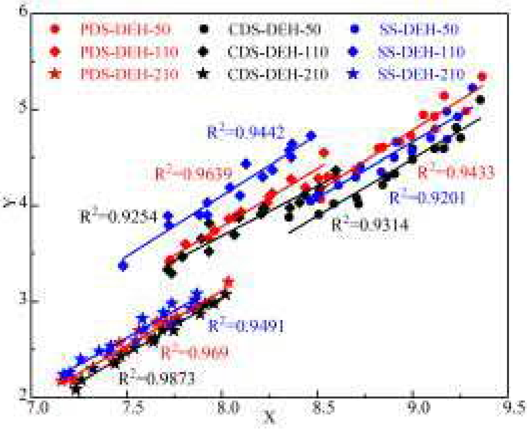

Fig. 8. Heat transfer correlation linear regression curves

Table 7 Regression parameters

Item	m	C	Item	m	C
PDS-DEH-50	1.28	$1.24 \cdot 10^{-3}$	SS-DEH-110	1.27	$2.37 \cdot 10^{-3}$
CDS-DEH-50	1.19	$2.03 \cdot 10^{-3}$	PDS-DEH-210	1.15	$2.28 \cdot 10^{-3}$
SS-DEH-50	1.16	$2.97 \cdot 10^{-3}$	CDS-DEH-210	1.18	$1.65 \cdot 10^{-3}$
PDS-DEH-110	1.21	$2.71 \cdot 10^{-3}$	SS-DEH-210	1.13	$2.90 \cdot 10^{-3}$
CDS-DEH-110	1.04	$9.38 \cdot 10^{-3}$			

3.4. Temperature distribution and heat transfer characteristics of heating rod

An electric heating rod is the key apparatus of a downhole electric heater. The temperature of the electric heating rod is related to the level of thermal damage on its surface, which determines the long-term operating stability of the downhole heater [36-38]. The temperature distribution characteristics of electric heating rods is explored in this section.

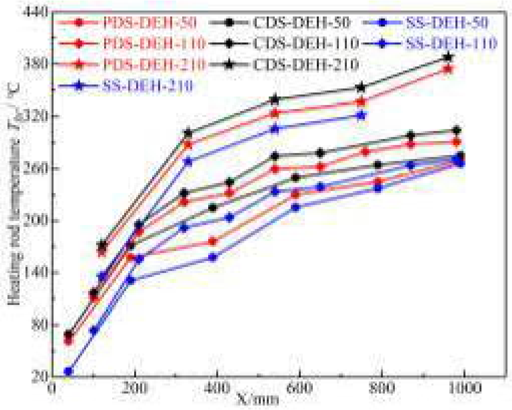

Fig. 9. Heating rod temperature curves along X-axis

Fig. 9 shows the heating rod temperatures along the X-axis. The heating rod temperature (T_{hr}) of the inlet section is the lowest, owing to the disordered air flow and low-temperature air. In fully developed section of the shell-side helical flow, the heat transfer temperature difference decreases gradually, therefore, T_{hr} increases gradually along the X-axis. In addition, the relative rank of T_{hr} is: CDS-DEH >PDS-DEH >SS-DEH (CDS-DEH and PDS-DEH are 3.45%-10.36% and 1.26%-6.55% higher than that of the SS-DEH, respectively). These results can be attributed to the following reasons. In the DS-DEH, air is preheated in outer shell-pass, therefore, the temperature difference of DS-DEH is lower than that of SS-DEH, leading to higher T_{hr} in DS-DEH. Compared with the PDS-DEH, the air absorbs more heat in outer shell-pass of CDS-DEH, and the heat transfer temperature difference in the same position is lower because the air temperature increases significantly; therefore, the outer shell temperature of CDS-DEH is higher than that of PDS-DEH. Additionally, it is discovered that in the same heater type, T_{hr} increases with the helical pitch values, which agree with results of previous studies regarding continuous helical baffle heaters.

The shell material of the electric heating rod is 304 stainless steel, and a high heating rod temperature will cause thermal damage [37,38]. It should be noted that based on the heating rod temperature distribution shown in Fig. 9 and the regression parameters presented in Table 7, the maximal heating rod temperature can be obtained. Therefore, the heating parameters of downhole heater can be adjusted to maintain the heating rod within a safe temperature range.

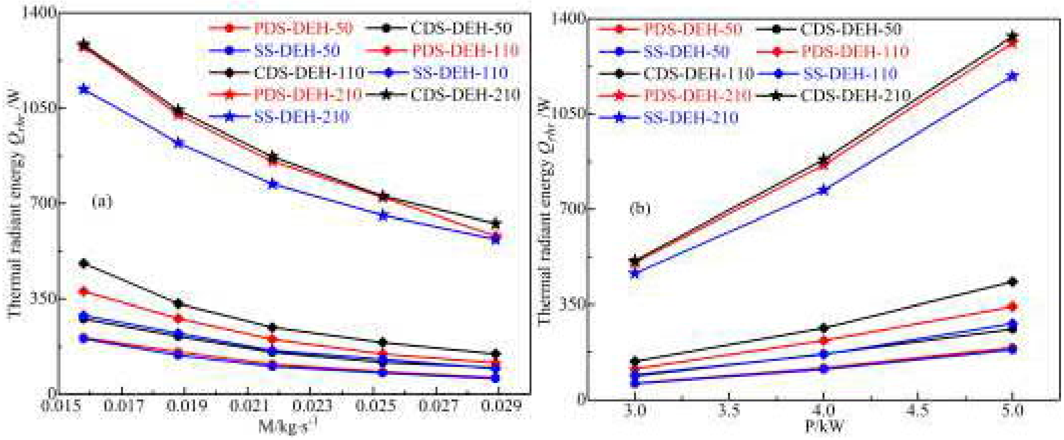

Fig. 10. Thermal radiant energy of heating rod versus mass flow rate and heating power

Fig. 10 presents the thermal radiant energy absorbed by shell-side air versus mass flow rate and heating power. It can be clearly seen that the thermal radiant energy absorbed by shell-side air decreases with the increase in the mass flow rate, whereas it shows the opposite trend for the heating power. Heaters with large helical pitch have greater variation rates. Additionally, the relative rank of thermal radiant energy absorbed by air is: DS-DEH> SS-DEH (DS-DEH is 1.03-1.70 times more than that of SS-DEH). The analysis shows that the shell-side air absorbs heat from the surface of the heating rod in two ways: forced convection and thermal radiation. Forced convection is the major heat transfer mode of heater shell-side. Heat transfer enhancement of heater shell-side is related to the helical pitch of continuous helical baffles. Although the heat transfer in shell-side is mainly forced convection, the contribution of radiation increases with the increase of helical pitch. Compared with SS-DEH, the air of DS-DEH is heated in the outer and inner shell-passes in sequence, therefore, the convection heat transfer temperature difference is lower in DS-DEH, hence, less heat is absorbed by the shell-side air in the form of convective heat transfer. Based on the above results, to increase the lifespan of downhole heaters, the contribution of radiant heat transfer in the shell-side should be as small as possible, so the continuous helical baffles with small helical pitch should be used.

3.5. Temperature distribution and heat transfer characteristics of heater shell

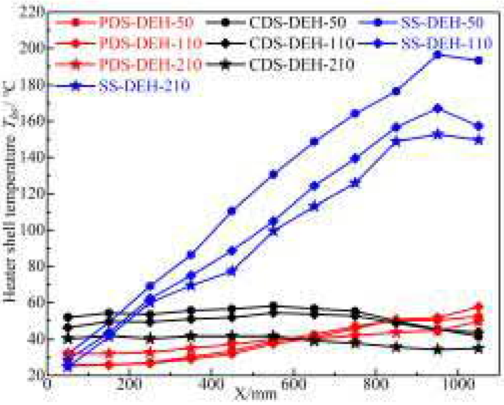

Fig. 11. Heater shell temperature curves along X-axis

The temperature distribution of heater shell (T_{hs}) along the X-axis is presented in Fig. 11. With the increase in the shell-side air temperature, T_{hs} increases along the X-axis. Furthermore, in double-shell heater, with the increase in air temperature in the outer shell-pass, the heat transfer temperature difference between the inner shell and the air in the outer shell-pass decreases, therefore, the growth rate of T_{hs} decreases. Moreover, in the outlet section of heater, no heating rod heats the air whilst heat is lost continuously in the heater shell; therefore, T_{hs} indicates a decreasing trend. The smaller is the helical pitch, the higher is the T_{hs}, and the faster the shell temperature decreases. Additionally, except for the temperatures in the gas injection section, the T_{hs} of the three types of heaters are ranked as follows: SS-DEH> CDS-DEH> PDS-DEH (CDS-DEH and PDS-DEH are 22.55%-80.00% and 55.94%-74.43% lower than that of the SS-DEH, respectively). The T_{hs} growth rate of SS-DEH is the largest, whereas the

T_{hs} of the double-shell heater increases more slowly. These results can be interpreted as follows. In the single-shell heater, the heat of heating rod is transferred directly from the shell-side air to the heater shell, whereas in the double-shell heater, the heat transfer sequence is the heating rod, inner shell-pass air, inner shell, outer shell-pass air, and outer shell. Meanwhile, because no heat transfer enhancement structure existed in the outer shell-pass, the air temperature distribution is lower owing to less heat absorbed by air and the temperature of outer shell is lower due to the smaller heat transfer temperature difference. Additionally, it is clear that in the same heater type, because more heat can be absorbed from the inner shell, the smaller is the pitch, the higher is the T_{hs}.

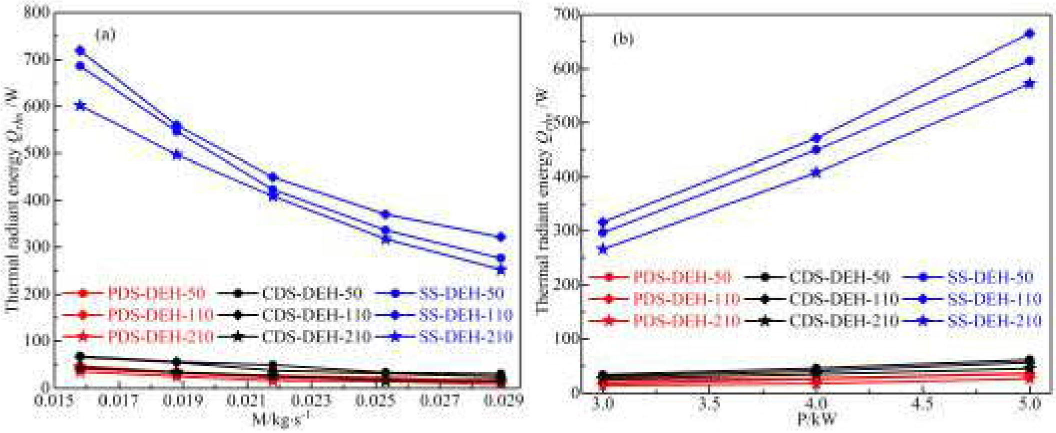

Fig. 12. Thermal radiant energy versus mass flow rate and heating power

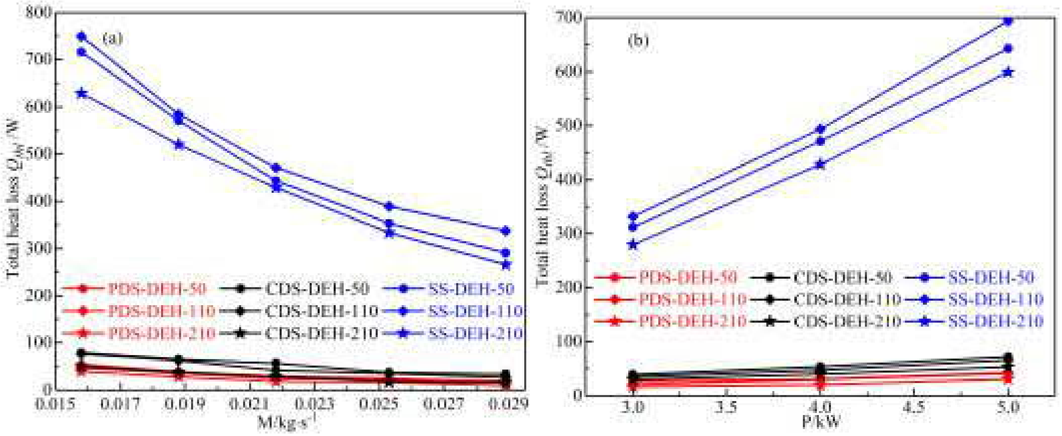

Fig. 13. Total heat loss versus mass flow rate and heating power

Figs. 12 and 13 show the variation trends of the thermal radiant energy and total heat loss of heater shell with the mass flow rate and heating power, respectively. Fig. 12 shows some resemblance to Fig. 10. The change rate of the SS-DEH is much larger than that of the DS-DEH, and that of the shell thermal radiant energy of DS-DEH is smaller. In addition, Fig. 12 indicates the relative rank of thermal radiant energy: SS-DEH> CDS-DEH> PDS-DEH (and the thermal radiant energy of SS-DEH is 8.86-30.10 times that of DS-DEH). Moreover, the variation trend of the total heat loss in Fig. 13 resembles that of the thermal radiant energy in Fig. 12. In the SS-DEH, the shell thermal radiant energy accounts for 94.84%-96.01% of total heat loss, whereas in the DS-DEH, it is only 85.10%-87.90%. Additionally, the total heat loss of DS-DEH is

87.16%-96.41% lower than that of SS-DEH.

The results shown in Figs. 12 and 13 can be explained as follows. According to Wien's displacement law [39], the lower is the temperature of the heater shell, the longer is the wavelength of the intense thermal radiation. According to the spectral emissive power distribution curve [39], the longer is the wavelength, the lower is the thermal radiant energy of heater shell. Because the shell temperature of SS-DEH is higher than that of DS-DEH, the radiation wavelength of heater shell is shorter and the entire radiation energy spectrum of the heater shell is reduced. In addition, the outer shell-pass air inflows from the high-temperature zone and flows out from the low-temperature zone in the inner shell-pass of CDS-DEH, whereas the opposite is shown in the PDS-DEH, which causes the shell temperature of the CDS-DEH to be higher than that of the PDS-DEH, so thermal radiation loss of CDS-DEH shell is higher than that of PDS-DEH. Although the increase in the inner shell-pass air mass flow rate enables the air to absorb more heat from the heating rod, this part of the heat is not proportional to the increase in the air mass flow rate; therefore, the outer shell-pass air temperature decreases, the outer shell radiation wavelength increases, and the shell thermal radiation energy decreases. According to the Stefan-Boltzmann law [39], the thermal radiant energy of the heater shell is positively correlated with the fourth power of the heater shell temperature. The transfer of thermal radiant energy does not depend on other media but is only related to the heater shell temperature; meanwhile, the natural convective heat transfer requires heat transfer media, which is not only related to heater shell temperature, but also to ambient temperature. Therefore, when ambient temperature is constant, the higher is the shell temperature, the greater is the rate of thermal radiant energy to the total heat loss.

3.6. Heating efficiency analysis

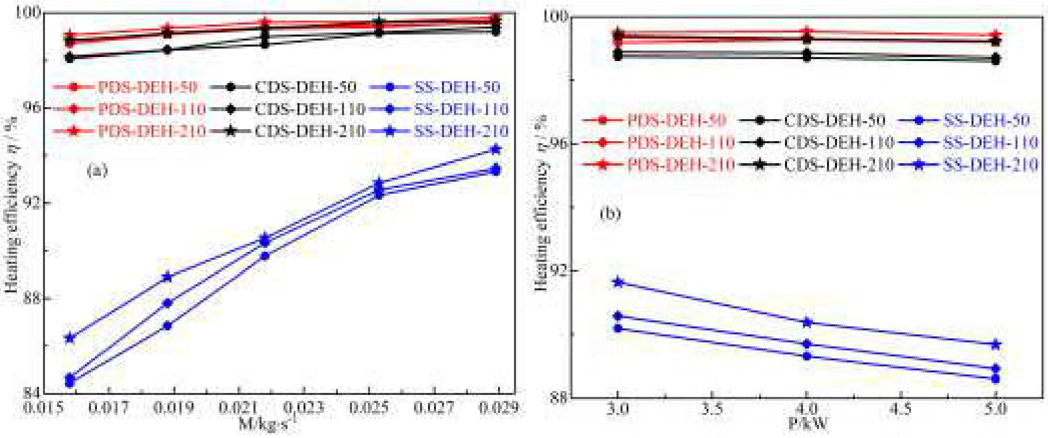

Fig. 14. Heating efficiency versus mass flow rate and heating power

Figs. 14 (a) and (b) show the variation trend of the heating efficiency versus mass flow rate and heating power, respectively. The heating efficiency (η) presented in Fig. 14 shows an opposite trend to Figs. 12 and 13. Furthermore, the relative rank of heating efficiency is: PDS-DEH> CDS-DEH> SS-DEH (the η of the PDS-DEH and CDS-DEH are 1.06-1.17 and 1.06-1.16 times that of the SS-DEH, respectively). It is clear that the mass flow rate and heating power do not significantly affect the heating efficiency of the DS-DEH, but affect that of the SS-DEH significantly. Additionally, within the test range, the η of the PDS-DEH, CDS-DEH, and SS-DEH are 98.69%-99.80%, 98.08%-99.65%, and 84.43%-94.25% respectively. Because the double-shell structure decreases the total heat loss of single-shell heater and reuses the heat loss of single-shell heater by preheating air in outer shell-pass, the η of the DS-DEH is higher than that of the SS-DEH.

Figs. 12-14 indicate that the thermal radiant energy dominates the total heat loss generated by the shell of SS-DEH. In addition, double-shell structure can effectively improve heating efficiency of downhole electric heater through reducing thermal radiant energy and natural convective heat transfer generated by shell of SS-DEH and through reusing the heat dissipated by the shell of SS-DEH. Moreover, as shown in Figs. 6 and 14, the higher is the outlet temperature, the lower is the η of SS-DEH. In in situ oil shale exploitations, the outlet temperature of downhole heater is higher than 400 ℃ and the η of the SS-DEH will be much lower than the η obtained in this study. Therefore, the double-shell structure is a good option for downhole electric heaters to reduce the operating cost of in situ exploitations of unconventional reservoirs.

4.Conclusions

A new type of downhole electric heater, which changes the flow path of shell-side air through a double-shell structure, was designed in this study. Subsequently, the thermal performance, total heat loss generated by heater shell, and heating efficiency of single- and double-shell heaters were experimentally investigated. Based on experimental results, the following conclusions can be obtained:

1. The effect of mass flow rate on heating rate is greater than that of heating power.
2. The SS-DEH has the largest comprehensive performance index. The difference in comprehensive performance index between the DS-DEH and SS-DEH depended on the helical pitch.
3. The heating rod temperatures of the CDS-DEH and PDS-DEH are 3.45%-10.36% and 1.26%-6.55% higher than that of the SS-DEH, respectively. Forced convection heat transfer is the major heat transfer mode in heater shell-side. As the helical pitch and heating power increase, and the mass flow rate decreases, the contribution of shell-side radiant heat transfer increases.
4. The heater shell temperatures of CDS-DEH and PDS-DEH are 54.10%-71.83% and 63.72%-75.37% lower than that of the SS-DEH, respectively. The heat loss of heater shell is mainly by radiant heat transfer, and the total heat loss of the DS-DEH is 87.16%-96.41% lower than that of the SS-DEH.
5. The double-shell structure effectively improves the heating efficiency of downhole electric heater, and the heating efficiency of the DS-DEH is 1.06-1.17 times that of the SS-DEH.

Nomenclature

A	Area, m^2	ρ	Density, kg/m^3
B	Helical pitch, m	μ	Dynamic viscosity, $kgm^{-1}s^{-1}$
d	Diameter, m	ν	Kinematic viscosity, m^2/s
F	Specific enthalpy, J/kg	η	Heating efficiency
f	Friction factor	ΔP	Pressure drop, Pa
g	Acceleration of gravity, m/s^2	Δt_e	Logarithmic temperature difference, K
G_r	Grashof number	Δt_{max}	Maximum temperature difference, K
h	Convective heat transfer coefficient, $W \cdot m^{-2} \cdot K^{-1}$	Δt_{min}	Minimum temperature difference, K
L	Length, m	Subscripts	
M	Mass flow rate, kg/s	amt	ambient temperature
N_u	Nusselt number	cl	characteristic length
P	Heating power, W	$conv$	natural convective
P_r	Prandtl number	ct	central tube
Q	Transferring heat, J	ehr	effective length of heating rod
R_a	Rayleigh number	hr	heating rod
R_e	Reynolds number	hs	heater shell
T	Temperature, K	in	inlet or inner
U_s	Characteristic velocity, m/s	min	minimum
Greek symbols		out	outlet or outer
λ	Thermal conductivity, W/(m·k)	rad	radiation
ε	Thermal radiation emissivity	s	shell-side
σ	Stefan-Boltzmann constant	thl	total heat loss
α	heat loss difference	$hbhl$	heat loss based on heat balance

Acknowledgments:

This research was funded by the National Key R&D Program of China (Grant No. 2019YFA0705502, Grant No. 2019YFA0705501), the Project of Jilin Province Development and Reform Commission of China, the Cooperaive Project between Universities and Jilin Province, China (Grant No. SF2017-5-1), the Program for JLU Science and Technology Innovative Research Team (Grant No. 2017TD-13), and the Fundamental Research Funds for the Central Universities. The authors would also like to thank the Academy of Finland for its partial support for this research (Grant No. 324023).

References

[1] Seyed Moein Elahi, Carlos E. Scott, Zhangxin Chen, Pedro Pereira-Almao. In situ upgrading and enhanced recovery of heavy oil from carbonate reservoirs using nano-catalysts: Upgrading reactions analysis[J]. Fuel,2019,252.

[2] Kun Guo, Hailong Li, Zhixin Yu. In situ heavy and extra-heavy oil recovery: A

review[J]. Fuel,2016,185.

[3] Minquan Dai, Zhaosheng Yu, Shiwen Fang, Xiaoqian Ma. Behaviors, product characteristics and kinetics of catalytic co-pyrolysis spirulina and oil shale[J]. Energy Conversion and Management,2019,192.

[4] Xianzhi Song,Chengkai Zhang,Yu Shi,Gensheng Li. Production performance of oil shale In situ conversion with multilateral wells[J]. Energy,2019,189.

[5] David W. Zhao, Jacky Wang, Ian D. Gates. Optimized solvent-aided steam-flooding strategy for recovery of thin heavy oil reservoirs[J]. Fuel,2013,112.

[6] Butler RM. A new approach to the modelling of steam-assisted gravity drainage. J Can Petrol Technol 1985;24(3):42–51.

[7] Wei Guo, Zhendong Wang, Zhongjin Sun, Youhong Sun, Xiaoshu Lü, Sunhua Deng, Lili Qu, Wang Yuan, Qiang Li. Experimental investigation on performance of downhole electric heaters with continuous helical baffles used in oil shale In situ pyrolysis[J]. Applied Thermal Engineering,2019,147.

[8] Hao Yang, Xiaoqiao Gao, Fansheng Xiong, Jialiang Zhang, Yanju Li. Temperature distribution simulation and optimization design of electric heater for In situ oil shale heating[J]. Oil Shale,2014,31(2).

[9] Z. Zhu, F. Zeng, G. Zhao, P. Laforge. Evaluation of the hybrid process of electrical resistive heating and solvent injection through numerical simulations[J]. Fuel,2013,105.

[10] Hassan Hassanzadeh, Thomas Harding. Analysis of conductive heat transfer during In situ electrical heating of oil sands[J]. Fuel,2016,178.

[11] Youhong Sun, Fengtian Bai, Xiaoshu Lü, Chunxia Jia, Qing Wang, Mingyi Guo, Qiang Li, Wei Guo. Kinetic study of Huadian oil shale combustion using a multi-stage parallel reaction model[J]. Energy,2015,82.

[12] Shifan Yang, Yaping Chen, Jiafeng Wu, Huaduo Gu. Influence of baffle configurations on flow and heat transfer characteristics of unilateral type helical baffle heat exchangers[J]. Applied Thermal Engineering,2018,133.

[13] Xinting Wang, Yunmin Liang, Yue Sun, Zhichun Liu, Wei Liu. Experimental and numerical investigation on shell-side performance of a double-shell-pass rod baffle heat exchanger[J]. International Journal of Heat and Mass Transfer,2019,132.

[14] Wei Wang, Yaning Zhang, Kwan-Soo Lee, Bingxi Li. Optimal design of a double pipe heat exchanger based on the outward helically corrugated tube[J]. International Journal of Heat and Mass Transfer,2019,135.

[15] Shui Ji, Wen-jing Du, Peng Wang, Lin Cheng, Y. Peles. Numerical Investigation on Double-shell-Pass Shell-and-Tube Heat Exchanger with Continuous Helical Baffles[J]. Journal of Thermodynamics,2011,2011.

[16] Jian-Feng Yang, Yuan-Sheng Lin, Han-Bing Ke, Min Zeng, Qiu-Wang Wang. Investigation on combined multiple shell-pass shell-and-tube heat exchanger with continuous helical baffles[J]. Energy,2016,115.

[17] Yang Lu, Ying Wang, Jing Zhang, Ying Xu, Guoqiang Li, Yongfa Zhang. Investigation on the catalytic effect of AAEMs in Zhundong coal on the combustion characteristics of Changji oil shale and its kinetics[J]. Energy,2019,178.

[18] Mao Mu, Xiangxin Han, Xiumin Jiang. Combined fluidized bed retorting and circulating fluidized bed combustion system of oil shale: 3. Exergy analysis[J].

Energy,2018,151.

[19] Xiangxin Han, Mengting Niu, Xiumin Jiang. Combined fluidized bed retorting and circulating fluidized bed combustion system of oil shale: 2. Energy and economic analysis[J]. Energy,2014,74.

[20] Ahmadali Gholami, Hussein A. Mohammed, Mazlan A. Wahid, Mehdi Khiadani. Parametric design exploration of fin-and-oval tube compact heat exchangers performance with a new type of corrugated fin patterns[J]. International Journal of Thermal Sciences,2019,144.

[21] Xin Chen, Huaizhi Han, Kwan-Soo Lee, Bingxi Li, Yaning Zhang. Turbulent heat transfer enhancement in a heat exchanger using asymmetrical outward convex corrugated tubes[J]. Nuclear Engineering and Design,2019,350.

[22] Simin Wang, Jian Wen, Huizhu Yang, Yulan Xue, Hanfei Tuo. Experimental investigation on heat transfer enhancement of a heat exchanger with helical baffles through blockage of triangle leakage zones[J]. Applied Thermal Engineering,2014,67(1-2).

[23] Aziz Hakan Altun, Orkun Ziylan. Experimental investigation of the effects of horizontally oriented vertical sinusoidal wavy fins on heat transfer performance in case of natural convection[J]. International Journal of Heat and Mass Transfer,2019,139.

[24] Lei Luo, Fengbo Wen, Lei Wang, Bengt Sundén, Songtao Wang. Thermal enhancement by using grooves and ribs combined with delta-winglet vortex generator in a solar receiver heat exchanger[J]. Applied Energy,2016,183.

[25] Ahmet Ali Sertkaya, Şefik Bilir, Suna Kargıcı. Experimental investigation of the effects of orientation angle on heat transfer performance of pin-finned surfaces in natural convection[J]. Energy,2011,36(3).

[26] E.M. Sparrow, S.B. Vemuri, Natural convection/radiation heat transfer from highly populated pin fin arrays [J]. Journal of Heat Transfer. 107 (1) (1985) 190–197.

[27] E.M. Sparrow, S.B. Vemuri, Orientation effects on natural convection / radiation heat transfer from highly populated pin - fin arrays[J]. International Journal of Heat and Mass Transfer. 29 (3) (1986) 359–368.

[28] W.H. McAdams, Heat Transmissions, third ed., McGraw Hill, New York, 1954, pp. 237–251.

[29] Seung-Hwan Yu, Daeseok Jang, Kwan-Soo Lee. Effect of radiation in a radial heat sink under natural convection[J]. International Journal of Heat and Mass Transfer,2011,55(1).

[30] M. Sheikholeslami, D.D. Ganji. Heat transfer enhancement in an air to water heat exchanger with discontinuous helical turbulators; experimental and numerical studies[J]. Energy,2016,116.

[31] Karima Boukhadia, Houari Ameur, Djamel Sahel, Mohamed Bozit. Effect of the perforation design on the fluid flow and heat transfer characteristics of a plate fin heat exchanger[J]. International Journal of Thermal Sciences,2018,126.

[32] Churchill S W, Bernstein M. A correlating equation for forced convection from gases and liquids to a circular cylinder in crossflow[J]. Asme Transactions Journal of Heat Transfer, 1977, 99(2):300-306.

[33] Gao B, Bi Q, Nie Z, et al. Experimental study of effects of baffle helix angle on

shell-side performance of shell-and-tube heat exchangers with discontinuous helical baffles[J]. Experimental Thermal & Fluid Science, 2015, 68:48-57.
[34] Moffat R J. Describing the uncertainties in experimental results[J]. Experimental Thermal & Fluid Science, 1988, 1(1):3-17.
[35] Kline S J. Describing Uncertainties in Single-Sample Experiments[J]. Mechanical Engineering, 1953, 75(1).
[36] Yanjun Wang, Ali Charbal, François Hild, Stéphane Roux, Ludovic Vincent. Crack initiation and propagation under thermal fatigue of austenitic stainless steel[J]. International Journal of Fatigue,2019,124.
[37] Yves Lejeail, Naoto Kasahara. Thermal fatigue evaluation of cylinders and plates subjected to fluid temperature fluctuations[J]. International Journal of Fatigue,2005,27(7).
[38] Elena Paffumi, Karl-Fredrik Nilsson, Zoltan Szaraz. Experimental and numerical assessment of thermal fatigue in 316 austenitic steel pipes[J]. Engineering Failure Analysis,2015,47.
[39] Shah R K, Sekulić D P. Fundamentals of Heat Exchanger Design[M]. 2003.